Theoretical and experimental investigation of the equation of state of boron plasmas

Shuai Zhang,[1,*] Burkhard Militzer,[2,3,†] Michelle C. Gregor,[1,‡] Kyle Caspersen,[1] Lin H. Yang,[1] Jim Gaffney,[1] Tadashi Ogitsu,[1] Damian Swift,[1] Amy Lazicki,[1] D. Erskine,[1] Richard A. London,[1] P. M. Celliers,[1] Joseph Nilsen,[1] Philip A. Sterne,[1] and Heather D. Whitley[1,§]

[1]*Lawrence Livermore National Laboratory, Livermore, California 94550, USA*

[2]*Department of Earth and Planetary Science, University of California, Berkeley, California 94720, USA*

[3]*Department of Astronomy, University of California, Berkeley, California 94720, USA*

(Received 29 April 2018; published 23 August 2018)

We report a theoretical equation of state (EOS) table for boron across a wide range of temperatures (5.1×10^4–5.2×10^8 K) and densities (0.25–49 g/cm^3) and experimental shock Hugoniot data at unprecedented high pressures (5608 ± 118 GPa). The calculations are performed with first-principles methods combining path-integral Monte Carlo (PIMC) at high temperatures and density-functional-theory molecular-dynamics (DFT-MD) methods at lower temperatures. PIMC and DFT-MD cross-validate each other by providing coherent EOS (difference <1.5 Hartree/boron in energy and <5% in pressure) at 5.1×10^5 K. The Hugoniot measurement is conducted at the National Ignition Facility using a planar shock platform. The pressure-density relation found in our shock experiment is on top of the shock Hugoniot profile predicted with our first-principles EOS and a semiempirical EOS table (LEOS 50). We investigate the self-diffusivity and the effect of thermal and pressure-driven ionization on the EOS and shock compression behavior in high-pressure and -temperature conditions. We also study the sensitivity of a polar direct-drive exploding pusher platform to pressure variations based on applying pressure multipliers to LEOS 50 and by utilizing a new EOS model based on our *ab initio* simulations via one-dimensional radiation-hydrodynamic calculations. The results are valuable for future theoretical and experimental studies and engineering design in high-energy density research.

DOI: 10.1103/PhysRevE.98.023205

I. INTRODUCTION

Recent experiments at the National Ignition Facility (NIF) have demonstrated the utility of large-diameter polar direct-drive exploding pushers (PDXP) as a low areal density platform for nucleosynthesis experiments [1], neutron source development, neutron and x-ray diagnostic calibration, and potentially as a candidate platform for heat transport studies [2]. Improving the platform for each of these respective uses requires consideration of various model uncertainties. Achieving a lower shell areal density during burn or obtaining additional data to help constrain estimates of this quantity in the nucleosynthesis experiments would simplify analysis of the charged particle data collected, while improving implosion symmetry is a necessary requirement if the platform is to be used to study heat transport. Variations in the ablators used in these experiments is one possible avenue that is currently under investigation. The use of glow-discharge polymer (GDP) as an ablator improves performance over smaller glass capsules [1], but its low tensile strength requires designs with shell thickness of about 15–20 μm in order to support gas fill pressures of around 8 bar. Higher tensile strength materials offer the option of producing thinner shells to support similar fill pressures, and reactions of ablator materials with neutrons and protons could potentially be used to obtain additional data to help quantify shell areal density at burn time. Some candidate materials with higher tensile strength include beryllium, boron, boron carbide, boron nitride, and high density carbon. For the purpose of conducting heat flow measurements, beryllium was ruled out as a candidate material due to the inclusion of argon within the capsule during the fabrication process [2]. Boron and nitrogen, which both undergo reactions with neutrons and protons, offer the potential for using additional nuclear reactions to better constrain the shell areal density during nuclear burn time, which could improve our overall understanding of the effects of the shell on the measured charged particles in the nucleosynthesis experiments. Boron is also interesting as an ablator material since its reactions with γ rays could be used to constrain ablator mix at burn time [3].

Radiation hydrodynamic simulations are the workhorse method for design and analysis of the inertial confinement fusion (ICF) and high-energy-density experiments. It has been demonstrated in many previous studies that the equation of state (EOS) of capsule ablator materials is an important component in indirect drive ICF performance [4–8], and EOS may also affect the implosion dynamics in the polar direct-drive platform, impacting not only capsule yield, but also the shell areal density during burn, and the electron-ion temperature separation in the gas. Thus, exploration of these materials as candidates for future PDXP-based experiments requires reasonable EOS models for use in radiation hydrodynamic simulations. In this paper, we examine the EOS of boron via

*zhang49@llnl.gov
†militzer@berkeley.edu
‡gregor3@llnl.gov
§whitley3@llnl.gov

both *ab initio* simulations and experimental measurements. We also examine its performance as an ablator in one-dimensional (1D) simulations of the PDXP platform, focusing on how variations in the EOS impact the computed yield and plasma conditions at burn time.

EOS models that are widely used in hydrodynamic simulation codes, such as the quotdian EOS (QEOS) [9,10], provide pressures and energies as smooth functions of temperature and density based on semiempirical methods, such as the Thomas-Fermi (TF) theory. The TF theory treats the plasma as a collection of nuclei that follow Boltzmann statistics and electrons that form continuous fluids and obey Fermi-Dirac statistics. This offers a good means to describe weakly coupled plasmas and materials at very high densities but is insufficient in describing many condensed matter solids and liquids, where bonding effects are significant. Additionally, at low-to-intermediate temperatures where atoms undergo partial ionization, the TF theory does not accurately capture the effects of shell ionization, which impacts the electronic contribution to the EOS of the material.

There has been continuous research in the development of improved methods for computing thermodynamic properties of materials, which has resulted in a variety of methods that can be applied to study EOS across a wide range of densities and temperatures. Several density-functional-theory–(DFT) based methods are appropriate to the study of dense plasmas, such as INFERNO [11], Purgatorio [12,13], orbital-free (OF) quantum molecular dynamics (MD) [14,15], and extended DFT [16]. Standard Kohn-Sham DFT-MD [17–19] has been widely applied for EOS studies of condensed matter as well as warm and hot, dense plasmas. It accounts for both the electronic shells and bonding effects and is thus superior to average-atom methods in situations where these types of strong many-body correlations are impactful to the EOS. However, the DFT-MD approach becomes computationally intractable at high temperatures because considerable numbers of partially occupied orbitals need to be considered. Other noteworthy approaches for plasmas and warm-dense matter EOS research include the activity-expansion method (ACTEX) [20–22] and many-body quantum Monte Carlo methods [23–29].

In ACTEX calculations, the plasma grand partition function is expanded as a series of terms describing the interactions between increasingly large numbers of fundamental plasma particles (electrons and boron nuclei in this case) [30,31]. Screened interactions and electron bound states arise naturally through a set of resummations, resulting in a convergent series which explicitly describes the formation of ions and molecules as well as quantum mechanical corrections to the EOS [32,33]. After resummation, electron-ion bound states are described in terms of their internal (Planck-Larkin) partition function which allows detailed atomic structure to be included in the EOS. This allows a clear link with other plasma microphysics quantities such as opacity, and ACTEX calculations are an important component of OPAL plasma opacity calculations [34]. ACTEX calculations, and OPAL opacities, have been extensively checked and found to be reliable even for quite strongly coupled plasmas [35]. The increasing complexity of terms as the number of interacting particles increases means that only the first few terms in the expansion are known, effectively limiting the ACTEX approach to high temperatures and moderate densities.

As a powerful tool initially developed for hydrogen [36], path-integral Monte Carlo (PIMC) has been successfully utilized to study plasmas from weak coupling to strongly coupled regimes with high accuracy. Recent developments by Militzer *et al.* [27,37] provide useful recipies for studying higher-Z plasmas. In the past 7 years, they have implemented the PIMC methods under the fixed-node approximation [38] and obtained the EOS for a series of elements (C, N, O, Ne, Na, Si) [27,37,39–43] and compounds (H_2O, LiF, hydrocarbons) [37,44–46] over a wide range of temperature and pressure conditions. The goal of the theoretical part of this paper is to apply these methods to calculate the EOS of boron and explore the effect on PDXP simulations in comparison with an older EOS model (LEOS 50) through hydrodynamic simulations.

Located in between metals and insulators in the periodic table, the structure and properties of boron have attracted wide interest in high-pressure physics. A number of studies have examined the stability relations of the α and the β phases [47–50], structural complexity of the β-rhombohedral phase [51,52], and phase transformation and melting of different boron polymorphs in high-pressure and -temperature conditions [53–58]. A phase diagram was proposed [59] based on theoretical and experimental studies at up to 300 GPa and showed five different crystalline phases, among which the α-Ga phase has not been experimentally verified so far [60]. There are experimental evidence for the existence of other phases (α, β, γ, and t), although questions remain on the exact phase boundary and the crystal structure of the t phase [52,60].

A considerable amount of study has been performed on boron at low densities, including DFT-MD simulations and x-ray radiography measurements on the structure, electronic, and thermodynamic properties of liquid boron [61,62], general chemical models for the the composition and transport properties of weakly coupled boron plasmas [63], isochoric EOS and resistivity of warm boron by combining closed vessel (EPI) experiments [64–66], DFT-MD [64], average-atom methods [67–69], and a chemical model (COMPTRA) [70]. In comparison to the vast progress in the low-temperature, high-pressure and the high-temperature, low-pressure regions of the boron phase diagram, studies at simultaneously high pressures and temperatures are rare. Until the year 2013, the only shock Hugoniot data available were at pressures below 112 GPa [71]. Recently, Le Pape *et al.* [72] used x-ray radiography to study the structure of shocked boron. They reported two experimental Hugoniot measurements (to the pressure of 400 GPa, which was the highest record to date) and ion-ion structure factors that are consistent with DFT-MD simulations. In this work, we conduct a dynamic compression experiment at NIF and extend the shock Hugoniot measurements of boron to a pressure of 14 times the previous record.

Hydrodynamic simulations of PDXP experiments require the EOS of the ablator materials along and off the Hugoniot curve at higher temperatures and pressures. The LEOS [9,10] and SESAME [73] EOS databases may be used, but it is unclear how their deviation from the true values affect the reliability of results in PDXP simulations, such as the neutron yield. In this work, we perform calculations of the boron

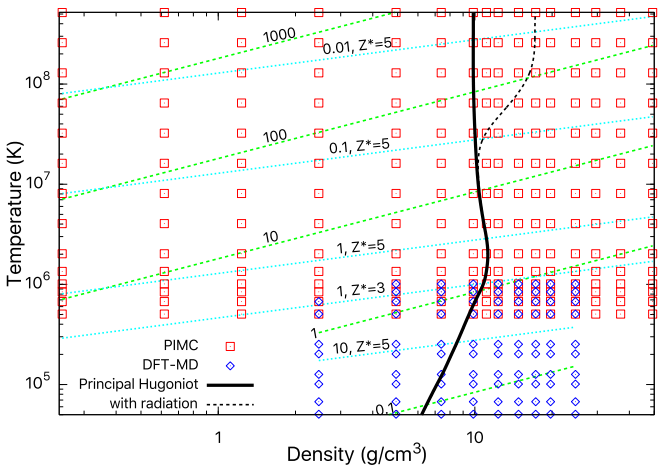

FIG. 1. Temperature-density conditions in our PIMC (red squares) and DFT-MD (blue diamonds) calculations are shown. The black curves depict the computed principal Hugoniot with (dashed) and without (solid) radiation correction [96] to the EOS. The dashed lines in green represent the conditions with different values of the degeneracy parameter, Θ, and the dotted lines in cyan denote the effective ionic coupling parameter, Γ. The Hugoniot curve is constructed by choosing the initial density to be the same as ρ_0 ($\sim$2.46 g/cm^3).

EOS over a wide range of temperatures and pressures. We extend PIMC simulations of dense boron plasmas from the "hot" (weak coupling and degeneracy) down to the "warm" region (coupling parameter and degeneracy both ≈ 1, see Fig. 1), where significant partial ionization of the K shell persists and standard DFT-MD simulations with frozen $1s$ core pseudopotential are not trustworthy. At relatively low temperatures, the system behaves like the usual condensed matter fluid, which can be reasonably well described within the DFT-MD framework. By pushing PIMC to low temperatures and DFT-MD to high temperatures, we get a coherent, first-principles EOS table for boron. We compare this table and the predicted shock compression profiles with LEOS and SESAME EOS tables for boron and perform hydrodynamic simulations to compare the effect of the different tables on the ICF performance.

The paper is organized as follows: Section II introduces the details of our simulation methods and experiment. Section III presents our EOS results, the calculated and measured shock Hugoniot data, and comparisons with other theories and models. Section IV discusses the atomic and electronic properties of boron plasmas, the ionization process, and PDXP performance sensitive to the EOS; finally, we conclude in Sec. V.

II. THEORY AND EXPERIMENT

A. First-principles simulation methods

Following the pioneering work applying PIMC to the simulations of real materials (hydrogen) [36] and recent development for pure carbon [37], hydrocarbons [45,46], and LiF [44], our PIMC simulations [74] utilize the fixed-node approximation [38] and treat both electrons and the nuclei as quantum paths that are cyclic in imaginary time $[0,\beta = 1/k_BT]$, where k_B is the Boltzmann constant. We use free-particle nodes to constrain the path to positive regions of the trial density matrix, which has been shown to work well for calculations of hydrogen [36,75–82], helium [83,84], and other first-row elements [37,39–41,44]. The Coulomb interactions are described via pair density matrices [85,86], which are evaluated at an imaginary time interval of [512 Hartree (Ha)] $^{-1}$. The nodal restriction is enforced in much smaller steps of [8192 Ha] $^{-1}$.

For our DFT-MD simulations, we choose the hardest available projected augmented wave (PAW) pseudopotential [87] for boron with core radii of 1.1 Bohr and frozen $1s^2$ electron, as provided in the Vienna *Ab initio* Simulation Package (VASP) [88]. We use the Perdew-Burke-Ernzerhof (PBE) [89] functional to describe the electronic exchange-correlation interactions, which is consistent with previous DFT calculations on solid boron [90–92]. We choose a large cutoff energy of 2000 eV for the plane-wave basis, and we use the Γ point to sample the Brillouin zone. The simulations are carried out in the NVT ensemble with a temperature-dependent time step of 0.05–0.55 fs, chosen to ensure reasonable conservation of energy. The temperature is regulated by a Nosé thermostat [93]. Each MD trajectory typically consists of 5000 steps to ensure that the system has reached equilibrium and to establish convergence of the energies and pressures. DFT-MD energies from VASP reported in this study are shifted by -24.596 Ha/B, the all-electron PBE energy of a single boron atom determined with OPIUM [94], in order to establish a consistent comparison with the all-electron PIMC energies.

Our PIMC calculations are performed at temperatures from 5.05×10^5 K to 5.17×10^8 K and densities ranging from 0.1 to 20 times the ambient density ρ_0 ($\sim$2.46 g/cm^3 based on that of the α phase [95]). We conduct DFT-MD simulations at temperatures between 5.05×10^4 K and 10^6 K, in order to check the PIMC calculations at the lowest temperatures. Due to limitations in applying the plane-wave basis for orbital expansion at low densities, and limitations in the applicability of the pseudopotential that freeze $1s^2$ electrons in the core at high densities, we consider a smaller number of densities (ρ_0–$10\rho_0$) in DFT-MD. These conditions are relevant to the dynamic shock compression experiments we have conducted at the NIF and span the range in which Kohn-Sham DFT-MD simulations are feasible. All PIMC calculations use 30-atom cubic cells, while in DFT-MD we consider both 30-atom cells and larger cells with 108 and 120 boron atoms to minimize the finite-size errors.

The temperature-density conditions included in this study are show in Fig. 1, along with contour lines corresponding to the ionic coupling parameter, $\Gamma = (Z^*e)^2/(ak_BT)$, and the electron degeneracy parameter, $\Theta = T/T_{\text{Fermi}}$, where T_{Fermi} is the Fermi temperature of free electrons, Z^* is the effective ion charge, k_B is the Boltzmann constant, $a = (3/4\pi n)^{1/3}$ is the average ionic distance, and n is the ion number density. Our PIMC and DFT-MD calculations span a wide range of conditions for the boron plasma, including weakly coupled ($\Gamma < 1$) plasmas, as well as collisional, strongly coupled ($\Gamma > 1$) and degenerate ($\Theta < 1$) plasmas. We utilize the simulation data to predict the principal shock Hugoniot profile over a range of pressures spanning 10 to 10^5 megabar (Mbar), as described in Sec. III B.

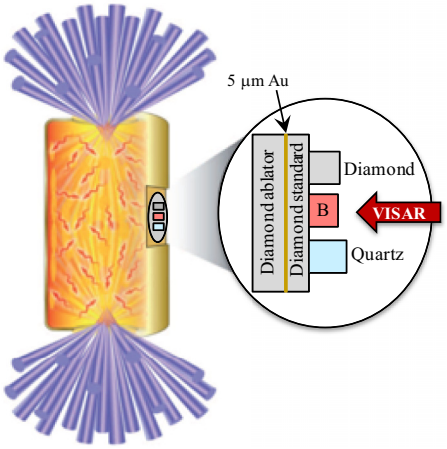

FIG. 2. Target design for the impedance-matching experiment at the NIF.

B. Shock Hugoniot experiment

An experiment to measure boron's Hugoniot near 50 Mbar was done at the NIF [97] at Lawrence Livermore National Laboratory (shot number N170801), using the impedance-matching technique [98]. As shown in Fig. 2, the target physics package was affixed to the side of a gold hohlraum and comprised a 200-μm-thick diamond ablator, 5-μm-thick gold preheat shield, and a 100-μm-thick diamond impedance-matching standard backing individual diamond, boron, and quartz samples. The optical-grade chemical vapor deposition diamond was polycrystalline with a density of 3.515 g/cm^3. The z-cut α-quartz and the boron had densities of 2.65 g/cm^3 and 2.31 g/cm^3, respectively. One hundred seventy-six laser beams in a 5-ns pulse with a total energy of 827 kJ produced an x-ray bath in the hohlraum with a peak radiation temperature of 250 eV as measured by the Dante multichannel soft x-ray spectrometer [99]. The x rays launched a strong, planar, and nearly steady shock wave, shown by measurements using a line-imaging velocity interferometer system for any reflector (VISAR) to vary $\sim \pm 3\%$ from its average velocity in the boron, that drove the samples to high pressures and temperatures.

The boron Hugoniot measurement was determined by impedance matching using the inferred shock velocities in the boron sample and diamond standard. Average shock velocities were determined from shock transit times, measured using VISAR [100], and the initial sample thicknesses, measured using a dual confocal microscope. The average velocities were further corrected for shock unsteadiness witnessed *in situ* in the transparent quartz sample [101–103]. The Hugoniot and release for the diamond standard were calculated using a tabular equation of state (LEOS 9061 [104]) created from a multiphase model based on DFT-MD and PIMC calculations [105]. The experimental Hugoniot data are given in Table I.

III. RESULTS

A. Equation of state

The first-principles EOS [106] computed with PIMC and DFT-MD calculations are shown in Figs. 3(a) and 3(b). The internal energies and pressures we computed using PIMC are consistent with those predicted by the ideal Fermi gas theory and the Debye-Hückel model in the high-temperature limit ($>1.6 \times 10^7$ K) where these models are valid. At lower temperatures, ideal Fermi gas theory and Debye-Hückel model predictions become increasingly higher and lower, respectively, than our PIMC values for both internal energy and pressure. This is easily understood due to the increased contribution from electron-electron and electron-ion correlations at lower temperature which render the high-temperature theories inadequate. The PIMC energies and pressures show the same trend as those from our DFT-MD simulations along all the nine isochores between ρ_0–$10\rho_0$.

The explicit inclusion of electronic shell structures leads to significant differences in the EOS of boron relative to the TF model, in particular at $T \leqslant 2 \times 10^6$ K. In comparison with our first-principles data, the LEOS 50 pressures differ by a variation -16.4% to 7.1%, and the internal energy differences are between -2.0 and 8.2 Ha/atom, at $T \leqslant 2.0 \times 10^6$ K. These differences lead to significantly different peak compression in the shock Hugoniot curves, as will be discussed in Sec. III B. At high temperatures ($T > 2 \times 10^6$ K), the relative differences in energies and pressures are small (between -3.1% and 0.5% in pressure and between -1% and 6% in internal energy).

With decreasing temperature from 10^6 to 5.05×10^5 K, we find improved agreement between PIMC and DFT-MD results in both internal energy and pressure [Figs. 3(c) and 3(d)]. We define a critical temperature of 5.05×10^5 K corresponding to the temperature above which significant ionization of the boron $1s^2$ core state is expected to render the pseudopotential calculation inaccurate. This critical temperature is lower than what we found recently for carbon in CH (10^6–2×10^6 K). This is due to the shallower $1s$ level in boron than in carbon. At the critical temperature, we find good consistency between PIMC and DFT-MD, with differences less than 1.5 Ha/B in energy and less than 5% in pressure.

The larger underestimation in energy and pressure by DFT-MD at higher densities and temperatures can be attributed to the failure of the pseudopotential approximation at these conditions. The significant compression at densities higher than $5\rho_0$ leads to the overlap of the nearby frozen cores,

TABLE I. Boron Hugoniot data from impedance matching (IM) with a diamond standard. Shock velocities (U_s) at the IM interface were measured *in situ* using VISAR for quartz (Q) and inferred using the nonsteady waves correction [101–103] for boron (B) and diamond (C). U_s^C and U_s^B were used in the IM analysis to determine the particle velocity (u_p), pressure (P), and density (ρ) on the boron Hugoniot.

U_s^Q (km/s)	U_s^C (km/s)	U_s^B (km/s)	u_p^B (km/s)	P^B (GPa)	ρ^B (g/cm^3)
55.18 ± 0.25	55.25 ± 0.74	58.71 ± 0.66	41.35 ± 0.82	5608 ± 118	7.811 ± 0.465

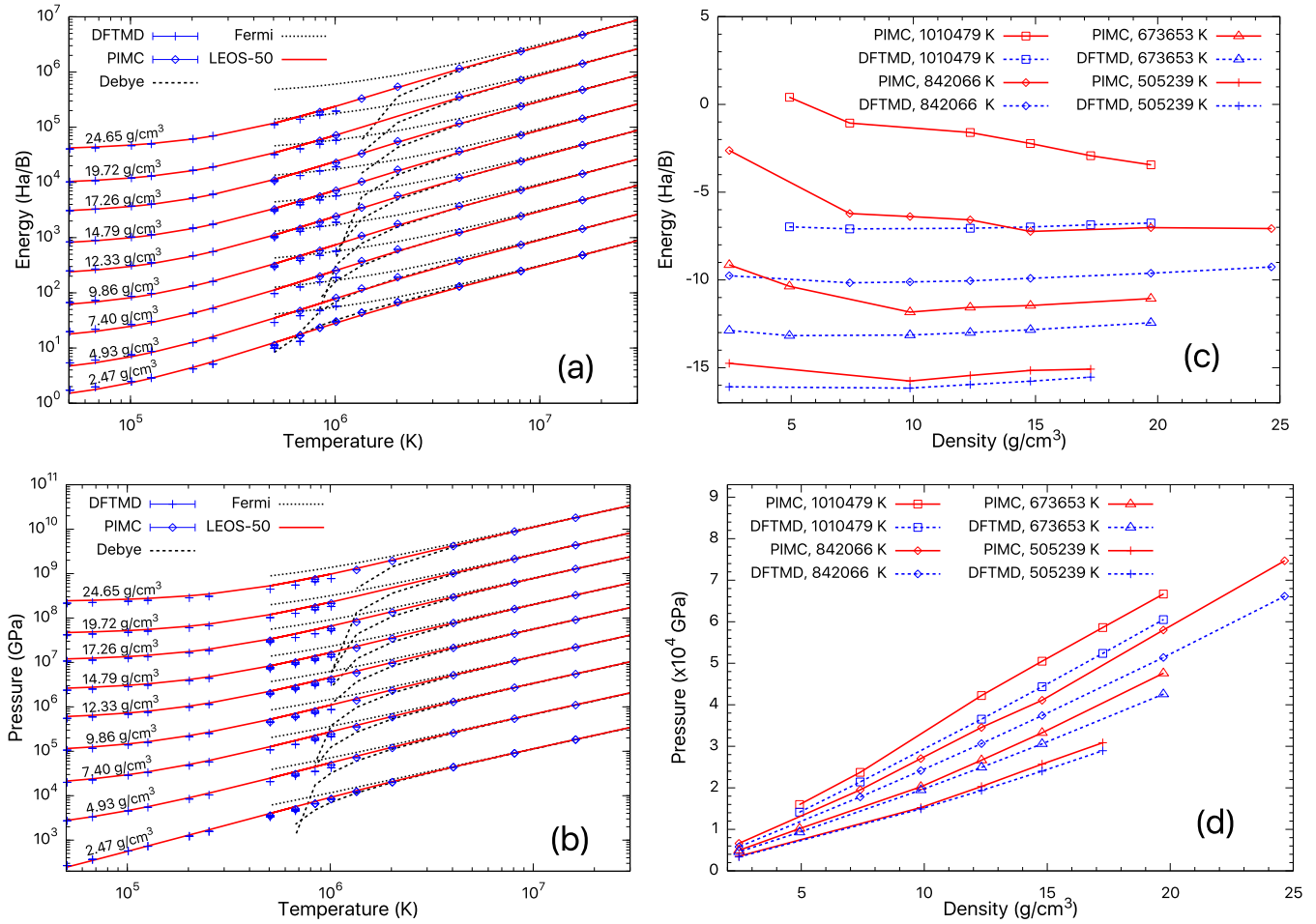

FIG. 3. (a) Energy- and (b) pressure-temperature EOS plots along isochores for boron from our PIMC and DFT-MD simulations. For comparison, the ideal Fermi-gas theory, Debye-Hückel model, and LEOS 50 are also shown. In (a), the LEOS 50 data have been aligned with DFT by setting their energies to be equal at 2.46 g/cm^3 and 0 K. Subplots (c) and (d) are the comparison in internal energy and pressure between PIMC and DFT-MD along four isotherms as functions of density. In subplots (a) and (b), results at different isochores have been shifted apart for clarity.

which makes the use of the pseudopotential inaccurate at these conditions. In previous studies, other authors have overcome the failure of the pseudopotential by constructing all-electron pseudopotentials that maintain accuracy up to higher temperatures and densities [15,107]. We note that the DFT-MD and PIMC EOS data reported here are in good agreement with the all-electron pseudopotential results [108].

B. Shock compression

During planar shock compression, the locus of the final (shocked) state (E, P, V) is related to the initial (preshocked) state (E_0, P_0, V_0) via the Rankine-Hugoniot equation [109]

$$(E - E_0) + \tfrac{1}{2}(P + P_0)(V - V_0) = 0, \qquad (1)$$

where E, P, and V denotes internal energy, pressure, and volume, respectively. Equation (1) allows for determining the P-V-T Hugoniot conditions with the EOS data in Sec. III A. We determine the initial energy E_0 and pressure P_0 by performing DFT-MD simulations at 300 K for α-boron with an initial density $\rho_0 = 2.46$ g/cm^3 throughout the manuscript, except when comparing with our experimental measurement for which E_0 and P_0 of β-boron with $\rho_0 = 2.31$ g/cm^3 (same as that of the sample used in the experiment) are used.

We plot the Hugoniot curves thus obtained in a pressure-compression ratio P-ρ/ρ_0 and a temperature-pressure T-P diagram in Fig. 4, and in a T-ρ diagram in Fig. 1. Our EOS based on PIMC calculations predict a maximum compression of 4.6 at 0.85 gigabar pressure and 2.0 million K temperature. In comparison, ACTEX calculations [110] predict boron to behave similarly while LEOS 50 and SESAME 2330 models predict it to be stiffer by 6.9% and 5.5%, respectively, at the maximum compression. The difference originates from the 1s shell ionization, which increases the compression ratio and is well captured in the PIMC simulations but not in the TF-based LEOS 50 and SESAME 2330 models. A similar deviation has been found for other low-Z systems, such as CH [45,46]. At lower temperatures, LEOS 50 predictions of the P-ρ/ρ_0 relation agree with our DFT-MD findings, while SESAME 2330 predicts boron to be softer by 6–10%. These are related to the specific details in constructing the cold curve and the thermal ionic parts in the EOS models.

The T-P Hugoniot curves predicted by the different methods are very similar. In comparison with our PIMC and

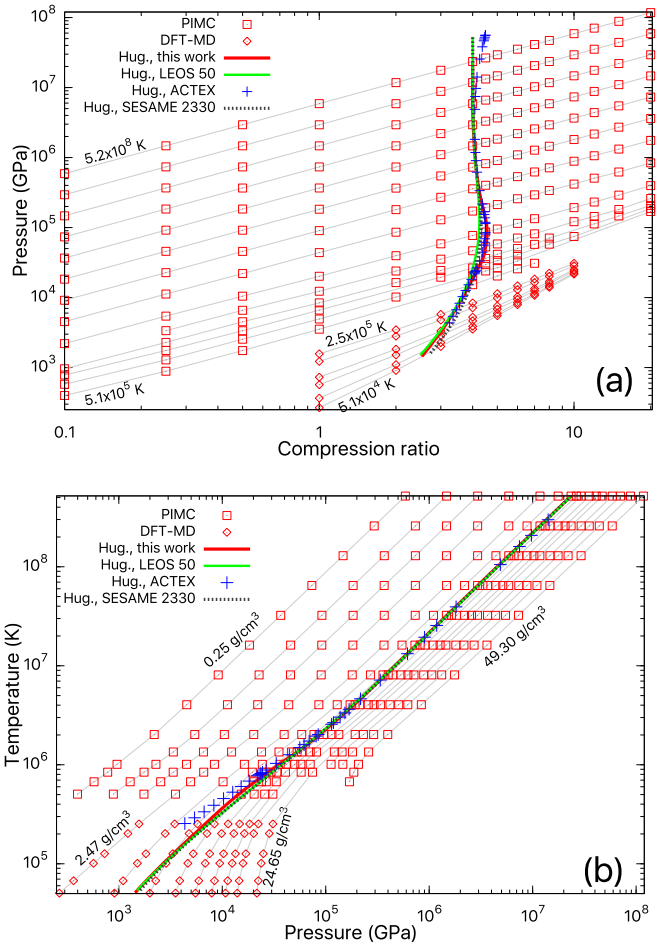

FIG. 4. Boron EOS and shock Hugoniot curves shown in (a) P-ρ/ρ_0 and (b) T-P plots. The Hugoniot results from LEOS 50, ACTEX, and SESAME 2330 are coplotted for comparison. Gray curves in panels (a) and (b) denote isotherms and isochores, respectively. The Hugoniot curves are constructed by choosing the initial density to be the same as ρ_0 ($\sim$2.46 g/cm^3). The difference between ACTEX and others in (a) at $P > 10^7$ GPa is because of the inclusion of electronic relativistic effects in ACTEX.

DFT-MD predictions in the 10^5–10^6 K regime, Thomas-Fermi-based LEOS 50 and SESAME 2330 slightly underestimate the temperature for fixed pressure, while ACTEX temperatures are higher. We suspect this is related to the K-shell occupations in the different theories and will put more detailed comparisons and discussions in a future publication.

The experimental boron Hugoniot data are summarized in Table I and compared with our theoretical predictions in a pressure-compression ratio plot (Fig. 5). The measured data point agrees perfectly with predictions by our first-principles calculations, X52 [111], ACTEX, and LEOS 50, but the prediction from the SESAME 2330 model is also consistent with the measurement if the 1 σ error bar in density is taken into account. The Hugoniot profiles by ACTEX and X52 are in excellent agreement with our PIMC and DFT-MD predictions. The minor mismatch in compression at 50–2000 Mbar is associated with the 1–2% uncertainty in our PIMC–DFT-MD Hugoniot curve because of the sparse data grid and nonsmooth numerical EOS data.

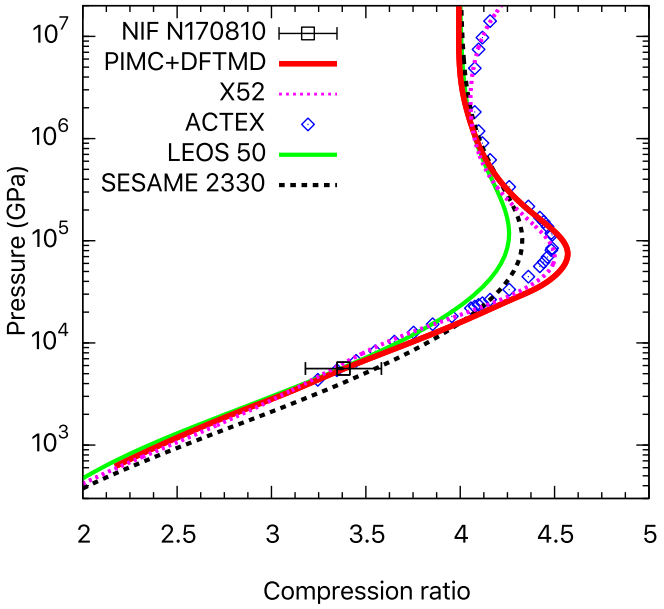

FIG. 5. Comparison of the experimental boron shock Hugoniot result with predictions from our first-principles EOS data and LEOS 50, SESAME 2330, X52 models, and ACTEX. The initial density for the PIMC–DFT-MD, LEOS 50, SESAME 2330, and X52 curves are 2.31 g/cm^3, i.e., the same as that of the experimental sample. The initial density for the ACTEX curve is 2.46 g/cm^3.

IV. DISCUSSION

A. Static and dynamic properties of boron plasmas

The EOS and shock compression of warm and hot dense matter can be understood from the atomic and electronic structures. Figure 6 compares the ionic radial distribution function $g(r)$ for boron at selected densities (3, 5, and 7 times ρ_0) and temperatures (6.74×10^4, 1.26×10^5, and 5.05×10^5 K) from our DFT-MD simulations. At 6.74×10^4 K, the $g(r)$ function shows a peak-valley feature between distances of 1.0–2.0 Å from the nucleus, which is characteristic of a bonding liquid. This feature gradually vanishes as temperature increases, indicating that the warm dense system being studied increasingly approaches an ideal gas, in spite of the significant coupling effect that exists (Fig. 1) and the fact that the atoms are not charge-neutral but partially ionized, as we will discuss below.

The pressure-driven and thermal ionization processes can be well described by comparing the $N(r)$ functions, which denote the average number of electrons within distance r from each nucleus, with the corresponding profile of the B^{3+} ionization state. $N(r)$ curves that are fully above the profile for B^{3+} are associated with fully occupied K shells, while those falling below indicate K-shell ionization. The results at 0.1×, 1.0×, 4.0×, and 20 × ρ_0 from our PIMC calculations are shown in Fig. 7. We find no observable ionization of the 1s states for $T < 0.5 \times 10^6$ K at $\rho > \rho_0$, which validates the use of the pseudopotential with a helium core in our DFT-MD simulations in these temperature and density conditions. As T exceeds 0.5×10^6 K, 1s electrons are excited and thus contribute to the total pressure and energy of the system, which

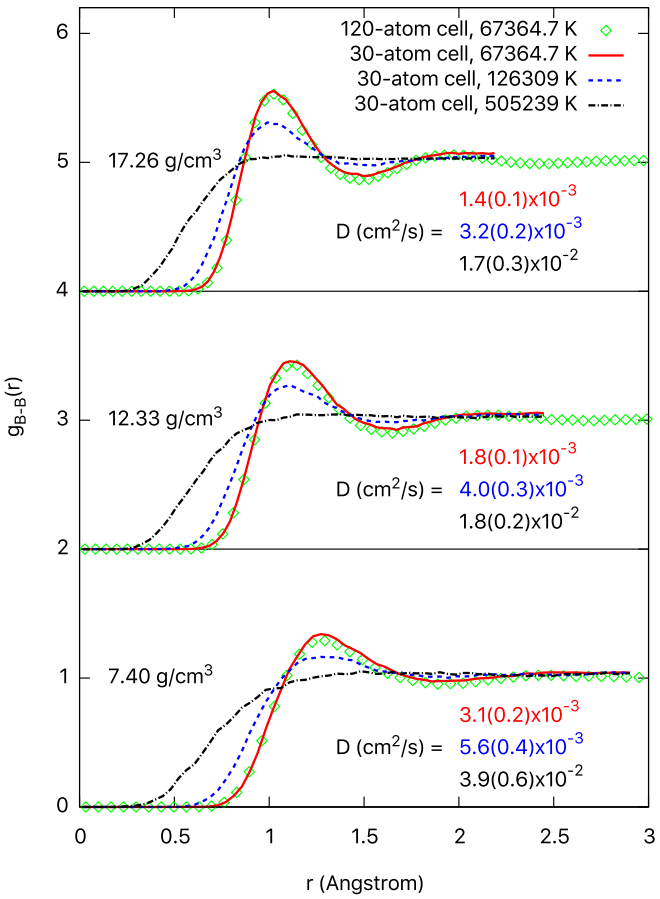

FIG. 6. Nuclear pair correlation function $g(r)$ of boron at three densities and three temperatures. The $g(r)$ curves analyzed based on MD simulations of 120-atom cells at 6736.47 K are coplotted for comparison. Curves at different densities have been off set for clarity. The consistency between $g(r)$ of 30- and 120-atom cells show negligible finite-size effect in describing the ionic structures. The numbers at the inset of each panel show the values of self diffusivity at the corresponding density. Numbers in parentheses denote the standard error of the corresponding data. Red, blue, and dark texts correspond to temperatures of 6.7×10^4, 1.3×10^5, and 5.1×10^5 K, respectively.

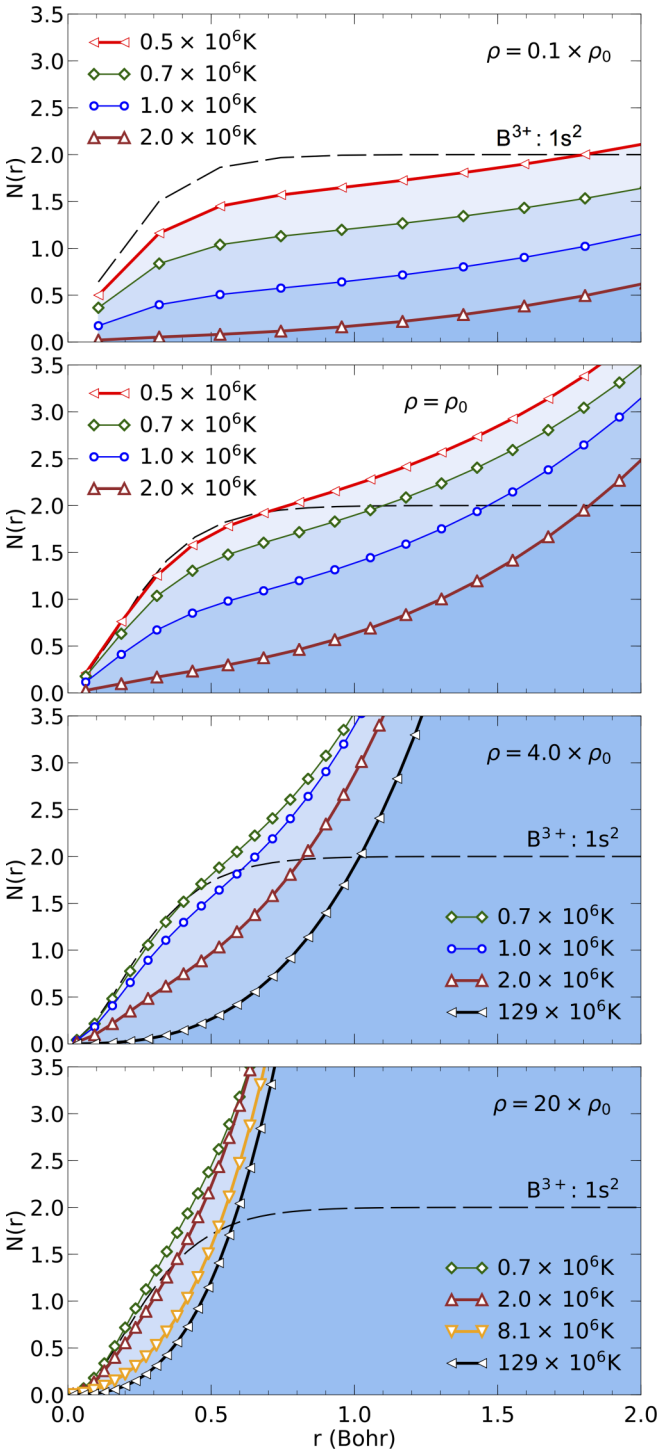

FIG. 7. The average number of electrons around each nucleus at different densities and a series of temperatures; $\rho_0 \approx 2.46\,\mathrm{g/cm^3}$. The long dashed curve denotes the corresponding profile of the isolated B^{3+} ion. The profile was derived by integrating the doubly occupied $1s$ orbitals that we computed with the GAMESS quantum chemistry code [112].

explains why both quantities are underestimated in DFT-MD, as has been shown in Fig. 3 and discussed in Sec. III A.

The $N(r)$ results also show that it requires higher temperatures for the K shell to reach the same degree of ionization at higher densities and that the same temperature change is associated with larger degrees of K-shell ionization at lower densities. Previous generalized chemical models [63] showed increasing fraction of B^{2+} particles at $T > 3.5 \times 10^4$ K and negligible K-shell ionization within the complete temperature range (up to 4.2×10^4 K) of their study for low-density ($0.094\,\mathrm{g/cm^3}$) boron plasmas, which remarkably agree with our findings here based on first-principles calculations.

In order to elucidate the physical origin of these observations, we compare the temperature dependence of the $1s$ binding energy E_b^{1s} with the chemical potential E_{CP} along four different isochores between $0.1\times$ and $20 \times \rho_0$. The results are obtained using the Purgatorio method [113] and are summarized in Fig. 8. As density increases, E_b^{1s} rises closer to the continuum level ($E = 0$). E_{CP} also increases with increasing density and in fact increases faster than E_b^{1s}. As a result, the Fermi occupation number of the $1s$ state

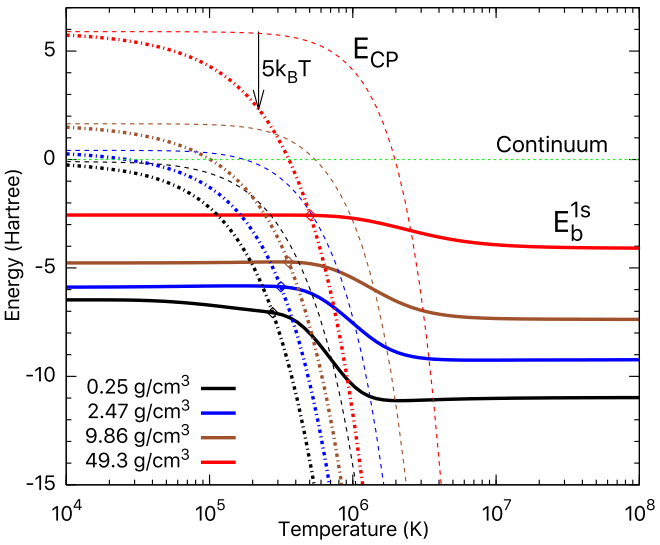

FIG. 8. Comparison of the $1s$ binding energy E_b^{1s} (solid curves) with the chemical potential $E_{\rm CP}$ (thin dashed curves) as functions of temperature at four densities. The data are obtained using the Purgatorio method. The dash-dotted curves represent $E_{\rm CP}$–$5k_BT$. The diamonds indicate the points at which the $1s$ level starts to be ionized (by 0.67%).

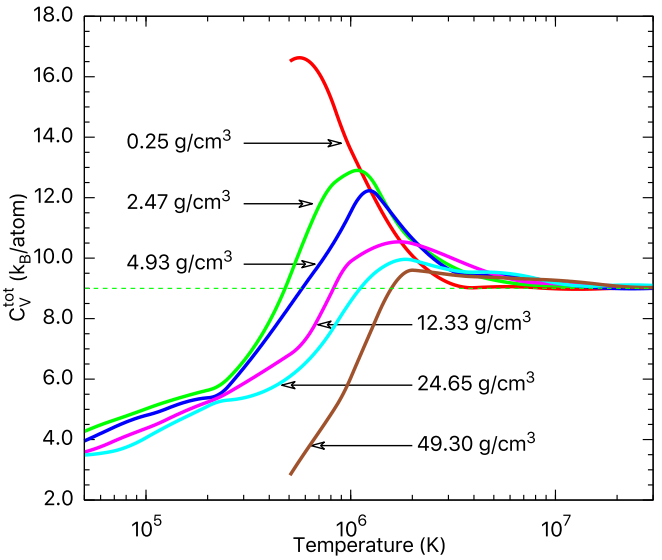

FIG. 9. Total heat capacity $C_V^{\rm tot} = (\partial E/\partial T)|_V$ of boron obtained from our DFT-MD and PIMC data along several isochores. All curves converge to the ideal-gas limit of $9k_B$/atom at high temperature.

actually increases with increasing density. At the temperature at which the E_b^{1s} and $E_{\rm CP}$ curves intersect, the $1s$ energy level has a Fermi occupation number of $1/2$. The dash-dotted curves in Fig. 8 plot the chemical potential minus $5k_BT$. The $1s$ level will have a Fermi occupation number of just 0.67% below full occupancy at the temperature at which these curves intersect the corresponding $1s$ energy levels. This intersection therefore indicates the critical temperature at which the $1s$ level starts to ionize. This intersection point shifts to higher temperature with increasing density, indicating that the ionization temperature increases with density, even though the $1s$ binding energy itself decreases. This accounts for the higher temperatures that are required for the K shell to reach the same degree of ionization at higher densities, as observed in Fig. 7. Purgatorio calculations of the K-shell occupation refines the critical temperature to 3.2×10^5–3.6×10^5 K at densities between ρ_0 and $4\rho_0$. We have also compared the Purgatorio results to that of DFT simulations of boron on a face-centered cubic lattice using a dual-projector optimized norm-conserving Vanderbilt (ONCV) [114,115] pseudopotential with core radius equaling 0.8 Bohr. The ONCV and the Purgatorio results on chemical potential, K-shell ionization energies, and K-shell occupation are in good agreement with each other.

The above findings about ionization are also consistent with the upshifting in energy, decreasing in magnitude, and expanding in width of the peak in heat capacity (Fig. 9) as density increases. The peaks originate from the excitation of $1s$ electrons of boron and appear at lower temperatures than that of carbon in CH with comparable densities [46]. This is because the K shell of boron is shallower than that of carbon.

We also estimate the self diffusion coefficient D for boron using $D = {\rm MSD}/6t$, where the MSD denotes the mean square displacement and t is the simulation time [116]. We obtained values of D that range between 8×10^{-4} and 0.05 cm^2/s at the temperatures (5×10^4–5×10^5 K) and densities (ρ_0–$10\rho_0$) that we performed DFT-MD simulations. We find the values of D (some shown in Fig. 6) monotonically increase with temperature and the specific volume. This is similar to what have been found for the diffusion of hydrogen in asymmetric binary ionic mixtures [117] and deuterium-tritium mixtures [118].

We note that accurate DFT-MD simulations of transport properties, such as diffusivity and viscosity, of one component plasmas across a wide coupling regime are useful because of the potential breakdown of laws for ordinary condensed matter (e.g., the Arrhenius relation) [119]. These studies also build the base for estimating the corresponding properties of mixtures [118] which, together with EOS approximations (e.g., average-atom or linear mixing approximation [45,46]), are important in characterizing multicomponent plasmas. However, such simulations require much more extended length of the MD trajectories and range of temperatures and densities in the more strongly coupled regime, which are beyond the scope of this work.

B. PDXP performance sensitivity to EOS

In Ref. [2], a 1D Ares [120,121] model for the PDXP platform with GDP capsules was developed to match the x-ray bang time and yield of N160920-003, N160920-005, and N160921-001. While we anticipate that changing the ablator in these experiments would necessitate recalibration of this model to match the performance of a new material, this model nonetheless offers a reasonable starting point for examining EOS sensitivity. The capsule in N160920-005 consisted of a 18-μm-thick GDP shell with an outer diameter of 2.95 mm, filled with 8 bar of D_2 gas and a trace amount of argon as a spectroscopic tracer. The implosion was driven by a 1.8-ns square pulse corresponding to a peak intensity of about 9.7×10^{14} W/cm^2. The model developed in Ref. [2] incorporates a

TABLE II. Polar direct-drive exploding pushers performance sensitivity to pressure change in boron EOS. We consider the LEOS 50 model, with pressure multipliers (p_{mult}) listed in parentheses, as well as the new X52 model. Corresponding data based on a GDP model are also shown for comparison.

EOS model (p_{mult})	Neutron yield	x-Ray bang time (ns)	Gas areal density (mg/cm^2)	Shell areal density (mg/cm^2)	Convergence ratio	Burn-averaged ion temperature (keV)
LEOS 50 (0.8)	2.15×10^{13}	2.10	3.53	2.75	3.80	16.2
LEOS 50 (1.0)	3.60×10^{13}	2.13	4.99	3.27	4.53	17.2
LEOS 50 (1.2)	5.70×10^{13}	2.18	7.38	4.12	5.60	17.5
X52 (1.0)	3.53×10^{13}	2.13	4.91	3.25	4.50	17.2
GDP model from Ref. [2]	2.14×10^{13}	3.17	17.5	29.1	12.29	7.80

multiplier on the energy delivered to the capsule, a flux limiter on the electron thermal conduction to account for inadequacies in the assumption of the diffusion model for heat transport, and a multiplier on the mass diffusion coefficient that is used to calibrate the multicomponent Navier-Stokes model for mixing of the capsule ablator into the deuterium fuel. The authors also modify the laser intensity used in the 1D simulations to account for geometric losses based on 2D Ares simulations. As discussed in Sec. III A, our *ab initio* simulations yield pressures that differ by up to 20% from the existing LEOS 50 table. The largest variations occur at temperatures between about 1×10^5 and 5×10^6 K, as shown in Fig. 3. In this regime, the electron thermal pressure is the largest contribution to the total pressure. We initially performed 1D Ares simulations using the LEOS 50 table with pressure multipliers of 0.8, 1.0, and 1.2 as a means of estimating the EOS sensitivity in a PDXP capsule using a boron ablator. We subsequently extended this sensitivity study to include the X52 model, which is based on Purgatorio and has been semiempirically fit to agree with the PIMC, DFT, and ACTEX isochores.

Because boron is substantially more dense than GDP (2.46 g/cm^3 compared to 1.05 g/cm^3), and because the higher tensile strength should allow for a thinner shell, we have chosen a thickness of 6 μm for the boron capsules. The use of a thinner ablator may reduce the effects of presumed mix in the capsules relative to the model calibrated for GDP. We therefore performed simulations of the boron PDXP model without the diffusive mix model, instead assuming a fall line model to estimate the impact of mix on the yield. The results of the EOS sensitivity study are shown in Table II. We find that applying pressure multipliers to LEOS 50 results in yield variations of -40% to $+58\%$. Higher ablator pressures result in higher gas areal density and higher convergence at burn time for very similar ion temperatures, and thus the impact on yield is generated primarily via higher compression of the D_2 gas as the pressure in the ablator increases. The shell areal density at the time of peak neutron production is also impacted by the pressure multiplier. In contrast, the new X52 model for boron gives results that are much more similar to LEOS 50, substantially narrowing the range of EOS-dependent uncertainty in the capsule yield.

The reason for the good agreement in capsule performance for LEOS 50 and X52 is that the pressure differences that were observed between the *ab initio* simulations and the LEOS 50 table are concommitant with differences in the internal energy, and the X52 model accounts for changes to both of these quantities. This demonstrates the importance of constraining both the pressure and the internal energy in EOS models that are used for radiation-hydrodynamic simulations.

For reference, the results from the model calculations in Ref. [2] are also listed in Table II. We find that the 1D Ares model predicts lower gas and much lower shell areal density at peak burn time for the boron ablator compared to GDP. This is because a larger portion of the thinner boron shell is ablated, allowing behavior more like a true exploding pusher than the thicker GDP ablator. The GDP design has a substantial amount of unablated plastic, leading to a lower implosion velocity, higher convergence, and lower ion temperatures relative to the boron ablator.

V. CONCLUSIONS

In this work, we present first-principles EOS results of boron using PIMC and DFT-MD simulations from temperatures of 5×10^4 K to 5.2×10^8 K. PIMC and DFT-MD cross-validates each other by showing remarkable consistency in the EOS ($<$1.5 Ha/B in total internal energy and $<$5% in total pressure) at 5×10^5 K. Our high-accurary EOS for boron provides an important base for future theoretical investigations of plasmas with boron.

We measured the boron Hugoniot at the highest pressure to date (56.1 ± 1.2 Mbar) in a dynamic compression experiment at NIF. The result shows excellent agreement with that obtained from our first-principles EOS data based on DFT-MD calculations. The experimental data point also agrees well with predictions by a TF model LEOS 50, the Purgatorio-based X52, and ACTEX calculations and is consistent with those by the TF-based SESAME 2330 if considering the 1σ error bar in density. In addition, our PIMC calculations predict a maximum compression of 4.6, which originates from K-shell ionization and is slightly larger than those predicted by TF models LEOS 50 and SESAME 2330. It requires more, high-precision experiments to test these predictions in these high-pressures and high-temperature regimes.

We investigated the PDXP performance sensitivity to the EOS with a 1D hydrodynamic model. The simulation results show that variations in pressure by -20% and 20% result in neutron yield variations of -40% to $+58\%$, respectively. In contrast, the new X52 model for boron gives results that are much more similar to LEOS 50, substantially narrowing the range of EOS-dependent uncertainty in the capsule yield. This demonstrates the importance of constraining both the pressure and the internal energy in EOS models that are used for radiation-hydrodynamic simulations.

ACKNOWLEDGMENTS

We thank C. Leland Ellison for providing support in running the 1D Ares model for the boron capsules. This research is supported by the U. S. Department of Energy, Grant No. DE-SC0016248. Computational support was mainly provided by the Blue Waters sustained-petascale computing project (NSF ACI 1640776), which is supported by the National Science Foundation (Awards No. OCI-0725070 and No. ACI-1238993) and the state of Illinois. Blue Waters is a joint effort of the University of Illinois at Urbana–Champaign and its National Center for Supercomputing Applications. S.Z. is partially supported by the PLS-Postdoctoral Grant of the Lawrence Livermore National Laboratory. S.Z. appreciates Dr. Babak Sadigh for helpful discussion about thermostat. This work was in part performed under the auspices of the U.S. Department of Energy by Lawrence Livermore National Laboratory under Contract No. DE-AC52-07NA27344.

[1] M. G. Johnson, D. T. Casey, M. Hohenberger, A. B. Zylstra, A. Bacher, C. R. Brune, R. M. Bionta, R. S. Craxton, C. L. Ellison, M. Farrell, J. A. Frenje, W. Garbett, E. M. Garcia, G. P. Grim, E. Hartouni, R. Hatarik, H. W. Herrmann, M. Hohensee, D. M. Holunga, M. Hoppe, M. Jackson, N. Kabadi, S. F. Khan, J. D. Kilkenny, T. R. Kohut, B. Lahmann, H. P. Le, C. K. Li, L. Masse, P. W. McKenty, D. P. McNabb, A. Nikroo, T. G. Parham, C. E. Parker, R. D. Petrasso, J. Pino, B. Remington, N. G. Rice, H. G. Rinderknecht, M. J. Rosenberg, J. Sanchez, D. B. Sayre, M. E. Schoff, C. M. Shuldberg, F. H. Séguin, H. Sio, Z. B. Walters, and H. D. Whitley, Phys. Plasmas **25**, 056303 (2018).

[2] C. L. Ellison, H. D. Whitley, C. R. D. Brown, S. R. Copeland, W. J. Garbett, H. P. Le, M. B. Schneider, Z. B. Walters, H. Chen, J. I. Castor, R. S. Craxton, M. G. Johnson, E. M. Garcia, F. R. Graziani, G. E. Kemp, C. M. Krauland, P. W. McKenty, B. Lahmann, J. E. Pino, M. S. Rubery, H. A. Scott, R. Shepherd, and H. Sio, Phys. Plasmas **25**, 072710 (2018).

[3] A. C. Hayes-Sterbenz, G. M. Hale, G. Jungman, and M. W. Paris, Los Alamos National Laboratory Report No. LA-UR-15-20627.

[4] B. Hammel, S. Haan, D. Clark, M. Edwards, S. Langer, M. Marinak, M. Patel, J. Salmonson, and H. Scott, High Energ. Dens. Phys. **6**, 171 (2010).

[5] H. F. Robey, J. D. Moody, P. M. Celliers, J. S. Ross, J. Ralph, S. Le Pape, L. Berzak Hopkins, T. Parham, J. Sater, E. R. Mapoles, D. M. Holunga, C. F. Walters, B. J. Haid, B. J. Kozioziemski, R. J. Dylla-Spears, K. G. Krauter, G. Frieders, G. Ross, M. W. Bowers, D. J. Strozzi, B. E. Yoxall, A. V. Hamza, B. Dzenitis, S. D. Bhandarkar, B. Young, B. M. Van Wonterghem, L. J. Atherton, O. L. Landen, M. J. Edwards, and T. R. Boehly, Phys. Rev. Lett. **111**, 065003 (2013).

[6] V. A. Smalyuk, D. T. Casey, D. S. Clark, M. J. Edwards, S. W. Haan, A. Hamza, D. E. Hoover, W. W. Hsing, O. Hurricane, J. D. Kilkenny, J. Kroll, O. L. Landen, A. Moore, A. Nikroo, L. Peterson, K. Raman, B. A. Remington, H. F. Robey, S. V. Weber, and K. Widmann, Phys. Rev. Lett. **112**, 185003 (2014).

[7] S. X. Hu, V. N. Goncharov, T. R. Boehly, R. L. McCrory, S. Skupsky, L. A. Collins, J. D. Kress, and B. Militzer, Phys. Plasmas **22**, 056304 (2015).

[8] S. X. Hu, L. A. Collins, V. N. Goncharov, J. D. Kress, R. L. McCrory, and S. Skupsky, Phys. Rev. E **92**, 043104 (2015).

[9] R. M. More, K. H. Warren, D. A. Young, and G. B. Zimmerman, Phys. Fluids **31**, 3059 (1988).

[10] D. A. Young and E. M. Corey, J. Appl. Phys. **78**, 3748 (1995).

[11] D. A. Liberman, Phys. Rev. B **20**, 4981 (1979).

[12] B. Wilson, V. Sonnad, P. Sterne, and W. Isaacs, J. Quant. Spectrosc. Radiat. Transfer **99**, 658 (2006).

[13] P. Sterne, S. Hansen, B. Wilson, and W. Isaacs, High Energ. Dens. Phys. **3**, 278 (2007).

[14] F. Lambert, J. Clérouin, and G. Zérah, Phys. Rev. E **73**, 016403 (2006).

[15] J.-F. Danel, L. Kazandjian, and G. Zérah, Phys. Plasmas **19**, 122712 (2012).

[16] S. Zhang, H. Wang, W. Kang, P. Zhang, and X. T. He, Phys. Plasmas **23**, 042707 (2016).

[17] P. Hohenberg and W. Kohn, Phys. Rev. **136**, B864 (1964).

[18] W. Kohn and L. J. Sham, Phys. Rev. **140**, A1133 (1965).

[19] N. D. Mermin, Phys. Rev. **137**, A1441 (1965).

[20] F. J. Rogers, Astrophys. J. **310**, 723 (1986).

[21] F. J. Rogers, *Equation of State in Astrophysics*, IAU Colloquium 147, G. Chabrier & E. Schatzman (eds.) (Cambridge Univeristy Press, Cambridge, 1994), pp. 16–42.

[22] F. J. Rogers, F. J. Swenson, and C. A. Iglesias, Astrophys. J. **456**, 902 (1996).

[23] E. L. Pollock and D. M. Ceperley, Phys. Rev. B **30**, 2555 (1984).

[24] E. L. Pollock, Comput. Phys. Commun. **52**, 49 (1988).

[25] D. M. Ceperley, Rev. Mod. Phys. **67**, 279 (1995).

[26] D. M. Ceperley, in *Monte Carlo and Molecular Dynamics of Condensed Matter Systems* (Editrice Compositori, Bologna, Italy, 1996), p. 443.

[27] B. Militzer and K. P. Driver, Phys. Rev. Lett. **115**, 176403 (2015).

[28] C. Pierleoni, M. A. Morales, G. Rillo, M. Holzmann, and D. M. Ceperley, Proc. Natl. Acad. Sci. USA **113**, 4953 (2016).

[29] G. Mazzola, R. Helled, and S. Sorella, Phys. Rev. Lett. **120**, 025701 (2018).

[30] F. J. Rogers and H. E. DeWitt, Phys. Rev. A **8**, 1061 (1973).

[31] F. J. Rogers, Phys. Rev. A **10**, 2441 (1974).

[32] F. J. Rogers, Phys. Rev. A **19**, 375 (1979).

[33] F. J. Rogers, Phys. Rev. A **24**, 1531 (1981).

[34] F. J. Rogers and C. A. Iglesias, Science **263**, 50 (1994).

[35] F. J. Rogers and D. A. Young, Phys. Rev. E **56**, 5876 (1997).

[36] C. Pierleoni, D. M. Ceperley, B. Bernu, and W. R. Magro, Phys. Rev. Lett. **73**, 2145 (1994).

[37] K. P. Driver and B. Militzer, Phys. Rev. Lett. **108**, 115502 (2012).

[38] D. M. Ceperley, J. Stat. Phys. **63**, 1237 (1991).

[39] K. P. Driver and B. Militzer, Phys. Rev. B **93**, 064101 (2016).

[40] K. P. Driver, F. Soubiran, S. Zhang, and B. Militzer, J. Chem. Phys. **143**, 164507 (2015).

[41] K. P. Driver and B. Militzer, Phys. Rev. B **91**, 045103 (2015).

[42] S. Zhang, K. P. Driver, F. Soubiran, and B. Militzer, High Energ. Dens. Phys. **21**, 16 (2016).

[43] S. Zhang, K. P. Driver, F. Soubiran, and B. Militzer, J. Chem. Phys. **146**, 074505 (2017).

[44] K. P. Driver and B. Militzer, Phys. Rev. E **95**, 043205 (2017).

[45] S. Zhang, K. P. Driver, F. Soubiran, and B. Militzer, Phys. Rev. E **96**, 013204 (2017).

[46] S. Zhang, B. Militzer, L. X. Benedict, F. Soubiran, P. A. Sterne, and K. P. Driver, J. Chem. Phys. **148**, 102318 (2018).

[47] A. Masago, K. Shirai, and H. Katayama-Yoshida, Phys. Rev. B **73**, 104102 (2006).

[48] S. Shang, Y. Wang, R. Arroyave, and Z.-K. Liu, Phys. Rev. B **75**, 092101 (2007).

[49] M. J. van Setten, M. A. Uijttewaal, G. A. de Wijs, and R. A. de Groot, J. Am. Chem. Soc. **129**, 2458 (2007).

[50] M. A. White, A. B. Cerqueira, C. A. Whitman, M. B. Johnson, and T. Ogitsu, Angew. Chem. **127**, 3697 (2015).

[51] T. Ogitsu, F. Gygi, J. Reed, Y. Motome, E. Schwegler, and G. Galli, J. Am. Chem. Soc. **131**, 1903 (2009).

[52] T. Ogitsu, E. Schwegler, and G. Galli, Chem. Rev. **113**, 3425 (2013).

[53] Y. Ma, C. T. Prewitt, G. Zou, H.-k. Mao, and R. J. Hemley, Phys. Rev. B **67**, 174116 (2003).

[54] E. Y. Zarechnaya, L. Dubrovinsky, N. Dubrovinskaia, Y. Filinchuk, D. Chernyshov, V. Dmitriev, N. Miyajima, A. El Goresy, H. F. Braun, S. Van Smaalen, I. Kantor, A. Kantor, V. Prakapenka, M. Hanfland, A. S. Mikhaylushkin, I. A. Abrikosov, and S. I. Simak, Phys. Rev. Lett. **102**, 185501 (2009).

[55] G. Parakhonskiy, N. Dubrovinskaia, E. Bykova, R. Wirth, and L. Dubrovinsky, Sci. Rep. **1**, 96 (2011).

[56] O. O. Kurakevych, Y. L. Godec, T. Hammouda, and C. Goujon, High Press. Res. **32**, 30 (2012).

[57] J. Qin, T. Irifune, H. Dekura, H. Ohfuji, N. Nishiyama, L. Lei, and T. Shinmei, Phys. Rev. B **85**, 014107 (2012).

[58] V. L. Solozhenko and O. O. Kurakevych, Sci. Rep. **3**, 2351 (2013).

[59] A. R. Oganov, J. Chen, C. Gatti, Y. Ma, Y. Ma, C. W. Glass, Z. Liu, T. Yu, O. O. Kurakevych, and V. L. Solozhenko, Nature **457**, 863 (2009).

[60] K. Shirai, Jpn. J. Appl. Phys. **56**, 05FA06 (2017).

[61] N. Vast, S. Bernard, and G. Zerah, Phys. Rev. B **52**, 4123 (1995).

[62] D. L. Price, A. Alatas, L. Hennet, N. Jakse, S. Krishnan, A. Pasturel, I. Pozdnyakova, M.-L. Saboungi, A. Said, R. Scheunemann, W. Schirmacher, and H. Sinn, Phys. Rev. B **79**, 134201 (2009).

[63] E. M. Apfelbaum, Contrib. Plasm. Phys. **53**, 317 (2013).

[64] J. Clérouin, P. Renaudin, and P. Noiret, Phys. Rev. E **77**, 026409 (2008).

[65] J. Clérouin, P. Noiret, P. Blottiau, V. Recoules, B. Siberchicot, P. Renaudin, C. Blancard, G. Faussurier, B. Holst, and C. E. Starrett, Phys. Plasmas **19**, 082702 (2012).

[66] J. Clérouin, C. Starrett, G. Faussurier, C. Blancard, P. Noiret, and P. Renaudin, Phys. Rev. E **82**, 046402 (2010).

[67] W. Johnson, C. Guet, and G. Bertsch, J. Quant. Spectrosc. Radiat. Transfer **99**, 327 (2006).

[68] G. Faussurier, C. Blancard, P. Cossé, and P. Renaudin, Phys. Plasmas **17**, 052707 (2010).

[69] C. Blancard and G. Faussurier, Phys. Rev. E **69**, 016409 (2004).

[70] S. Kuhlbrodt, B. Holst, and R. Redmer, Contrib. Plasm. Phys. **45**, 73 (2005).

[71] LASL Shock Hugoniot Data, edited by S. P. Marsh (University of California Press, Berkeley, 1980).

[72] S. Le Pape, A. A. Correa, C. Fortmann, P. Neumayer, T. Döppner, P. Davis, T. Ma, L. Divol, K.-U. Plagemann, E. Schwegler, R. Redmer, and S. Glenzer, New J. Phys. **15**, 085011 (2013).

[73] S. P. Lyon and J. D. Johnson (eds.,) SESAME: The Los Alamos National Laboratory Equation of State Database (Group T-1, Report No. LA-UR-92-3407, 1992).

[74] B. Militzer, Ph.D. Thesis, University of Illinois at Urbana-Champaign (2000).

[75] W. R. Magro, D. M. Ceperley, C. Pierleoni, and B. Bernu, Phys. Rev. Lett. **76**, 1240 (1996).

[76] B. Militzer and D. M. Ceperley, Phys. Rev. E **63**, 066404 (2001).

[77] B. Militzer, D. M. Ceperley, J. D. Kress, J. D. Johnson, L. A. Collins, and S. Mazevet, Phys. Rev. Lett. **87**, 275502 (2001).

[78] S. X. Hu, B. Militzer, V. N. Goncharov, and S. Skupsky, Phys. Rev. Lett. **104**, 235003 (2010).

[79] B. Militzer and D. M. Ceperley, Phys. Rev. Lett. **85**, 1890 (2000).

[80] S. X. Hu, B. Militzer, V. N. Goncharov, and S. Skupsky, Phys. Rev. B **84**, 224109 (2011).

[81] B. Militzer, W. Magro, and D. Ceperley, Contrib. Plasma Phys. **39**, 151 (1999).

[82] B. Militzer and R. L. Graham, J. Phys. Chem. Solids **67**, 2136 (2006).

[83] B. Militzer, Phys. Rev. Lett. **97**, 175501 (2006).

[84] B. Militzer, J. Low Temp. Phys. **139**, 739 (2005).

[85] V. Natoli and D. M. Ceperley, J. Comput. Phys. **117**, 171 (1995).

[86] B. Militzer, Comput. Phys. Commun. **204**, 88 (2016).

[87] P. E. Blöchl, O. Jepsen, and O. K. Andersen, Phys. Rev. B **49**, 16223 (1994).

[88] G. Kresse and J. Furthmüller, Phys. Rev. B **54**, 11169 (1996).

[89] J. P. Perdew, K. Burke, and M. Ernzerhof, Phys. Rev. Lett. **77**, 3865 (1996).

[90] T. Ogitsu, F. Gygi, J. Reed, M. Udagawa, Y. Motome, E. Schwegler, and G. Galli, Phys. Rev. B **81**, 020102 (2010).

[91] D. L. V. K. Prasad, M. M. Balakrishnarajan, and E. D. Jemmis, Phys. Rev. B **72**, 195102 (2005).

[92] B. Siberchicot, Phys. Rev. B **79**, 224101 (2009).

[93] S. Nosé, J. Chem. Phys. **81**, 511 (1984).

[94] See http://opium.sourceforge.net for information about the OPIUM code.

[95] G. Will and B. Kiefer, Z. Anorg. Allg. Chem. **627**, 2100 (2001).

[96] The radiation correction was added to our first-principles EOS by considering an ideal black body scenario. Details about the way of adding this correction have been shown in our previous work (Ref. [43]). In comparison with electronic relativistic effects, the radiation correction becomes evident along the Hugoniot curve at a lower temperature; whereas in both cases the compression ratio approaches the limit of 7 at high temperature.

[97] E. I. Moses, R. N. Boyd, B. A. Remington, C. J. Keane, and R. Al-Ayat, Phys. Plasmas **16**, 041006 (2009).

[98] L. V. Al'tshuler, K. K. Krupnikov, and M. I. Brazhnik, Sov. Phys. JETP **34**, 614 (1958).

[99] E. L. Dewald, K. M. Campbell, R. E. Turner, J. P. Holder, O. L. Landen, S. H. Glenzer, R. L. Kauffman, L. J. Suter, M. Landon, M. Rhodes, and D. Lee, Rev. Sci. Instrum. **75**, 3759 (2004).

[100] P. M. Celliers, D. K. Bradley, G. W. Collins, D. G. Hicks, T. R. Boehly, and W. J. Armstrong, Rev. Sci. Instrum. **75**, 4916 (2004).

[101] D. E. Fratanduono, D. H. Munro, P. M. Celliers, and G. W. Collins, J. Appl. Phys. **116**, 033517 (2014).

[102] M. C. Gregor, D. E. Fratanduono, C. A. McCoy, D. N. Polsin, A. Sorce, J. R. Rygg, G. W. Collins, T. Braun, P. M. Celliers, J. H. Eggert, D. D. Meyerhofer, and T. R. Boehly, Phys. Rev. B **95**, 144114 (2017).

[103] D. E. Fratanduono, P. M. Celliers, D. G. Braun, P. A. Sterne, S. Hamel, A. Shamp, E. Zurek, K. J. Wu, A. E. Lazicki, M. Millot, and G. W. Collins, Phys. Rev. B **94**, 184107 (2016).

[104] We have tried reanalyzing our data using three different diamond EOS models, including LEOS 64, LEOS 65, and SESAME 7834 and found the spread in the boron Hugoniot points using the three diamond tables is within the error bar.

[105] L. X. Benedict, K. P. Driver, S. Hamel, B. Militzer, T. Qi, A. A. Correa, A. Saul, and E. Schwegler, Phys. Rev. B **89**, 224109 (2014).

[106] See Supplemental Material at http://link.aps.org/supplemental/10.1103/PhysRevE.98.023205 for the EOS data table of boron from this study.

[107] S. Mazevet, F. Lambert, F. Bottin, G. Zérah, and J. Clérouin, Phys. Rev. E **75**, 056404 (2007).

[108] We perform DFT-MD simulations using our plane-wave pseudopotential code [122] and a self-built all-electron ONCV [114,115] pseudopotential at selected densities and temperatures in the range of 8.71–87.08 eV. The ONCV pseudopotential has a small core radius of 0.8 Bohr. The simulations are based on 30-atom cells and the initial configurations are from our VASP simulations at corresponding temperatures and densities. Our results show the pressure between ONCV and VASP calculations generally agree very well at $T = 8.71$ eV. We only find differences of up to 1% for densities between 15 and 25 g/cm^3. At $T = 21.77$ eV, the pressure difference gradually increases from 0 to 1.5% as densities increases from 5 to 12.5 g/cm^3. The difference further increases to 6% at 25 g/cm^3, which suggests that the VASP-PAW frozen-core pseudopotential works well for all densities at low temperatures, and only becomes less reliable at the high temperature of 21.77 eV for densities higher than 12.5 g/cm^3 at which the core of neighbored atoms overlap. At temperatures of 43.54 and 87.08 eV, the all-electron ONCV pressures are well consistent with PIMC values (differences are within 2%).

[109] M. A. Meyers, *Dynamic Behavior of Materials* (Wiley, New York, 1994).

[110] Our ACTEX calculations are limited to $T > 20$ eV at which point the two-particle contribution to the pressure becomes comparable to the Saha term. This is sufficient to capture the peak in the compression on the Hugoniot as well as significant deviation from ideal Saha behavior.

[111] X52 is a new Purgatorio-based boron EOS model. It was constructed by following the QEOS approach [9,10] and decomposing the free energy into contributions from the cold curve, ion-thermal, and electron-thermal parts. The model parameters were constrained by our first-principles EOS data using DFT-MD, PIMC, and ACTEX.

[112] See http://www.msg.ameslab.gov/gamess/ for information about the GAMESS code.

[113] Our Purgatorio calculations on boron use the Coulomb potential and the Hedin-Lundqvist [123] form of exchange-correlation functional under local density approximation (LDA).

[114] D. R. Hamann, Phys. Rev. B **88**, 085117 (2013).

[115] D. R. Hamann, Phys. Rev. B **95**, 239906(E) (2017).

[116] A good reference on this can be found in Chap. 3 of the lecture notes by K. Schulten and I. Kosztin: http://www.ks.uiuc.edu/Services/Class/NSM.pdf.

[117] H. D. Whitley, W. E. Alley, W. H. Cabot, J. I. Castor, J. Nilsen, and H. E. DeWitt, Contrib. Plasma Phys. **55**, 413 (2015).

[118] J. D. Kress, J. S. Cohen, D. A. Horner, F. Lambert, and L. A. Collins, Phys. Rev. E **82**, 036404 (2010).

[119] J. Daligault, Phys. Rev. Lett. **96**, 065003 (2006).

[120] R. M. Darlington, T. L. McAbee, and G. Rodrigue, Comput. Phys. Commun. **135**, 58 (2001).

[121] B. E. Morgan and J. A. Greenough, Shock Waves **26**, 355 (2016).

[122] L. H. Yang, R. Q. Hood, J. E. Pask, and J. E. Klepeis, J. Comput,-Aided Mater. Des. **14**, 337 (2007).

[123] L. Hedin and B. I. Lundqvist, J. Phys. C **4**, 2064 (1971).